



Nanoscale

DNA self-assembled Au nanoparticle clusters on the silver nanorod array for high-sensitive and multiplex detection of cancer-related biomarkers

Journal:	<i>Nanoscale</i>
Manuscript ID	NR-ART-01-2022-000133.R1
Article Type:	Paper
Date Submitted by the Author:	14-Feb-2022
Complete List of Authors:	<p>Yang, Yanjun ; Nanjing University of Posts and Telecommunications, Institute of Advanced Materials; University of Georgia, School of Electrical and Computer Engineering</p> <p>Song, Chunyuan; Nanjing University of Posts and Telecommunications</p> <p>Zhang, Jingjing; Nanjing University of Posts and Telecommunications, Institute of Advanced Materials</p> <p>Chao, Jie; Nanjing University of Posts and Telecommunications</p> <p>Luong, Hoang Mai ; University of Georgia, Department of Physics and Astronomy</p> <p>Zhao, Yiping; University of Georgia, Department of Physics and Astronomy</p> <p>Wang, Lian-Hui; Nanjing University of Posts and Telecommunications, Institute of Advanced Materials</p>

SCHOLARONE™
Manuscripts

ARTICLE

DNA self-assembled Au nanoparticle clusters on the silver nanorod array for high-sensitive and multiplex detection of cancer-related biomarkers

Yanjun Yang^{a,c}, Chunyuan Song^{*a}, Jingjing Zhang^a, Jie Chao^a, Hoang Mai Luong^b, Yiping Zhao^{*b}, Lianhui Wang^{*a}

Received 00th January 20xx,
Accepted 00th January 20xx

DOI: 10.1039/x0xx00000x

To sensitively detect multiple and cross-species disease-related targets from a single biological sample in a quick and reliable manner is of high importance in accurately diagnosing and monitoring diseases. Herein, a surface-enhanced Raman scattering (SERS) sensor based on functionalized multiple-armed tetrahedral DNA nanostructures (FMTDNs) immobilized silver nanorod (AgNR) array substrate and Au nanoparticle (AuNP) SERS tags is constructed to achieve both multiplex detection and enhanced sensitivity using a sandwich strategy. The sensor can achieve single, dual, and triple biomarker detections of three lung cancer-related nucleic acid and protein biomarkers, i.e., miRNA-21, miRNA-486 and carcinoembryonic antigen (CEA) in human serum. The enhanced SERS signals in multiplex detections are due to the DNA self-assembled AuNP clusters on the silver nanorod array during the assay, and the experimentally obtained relative enhancement factor ratios, 150 for AuNP dimers and 840 for AuNP trimers, qualitatively agree with the numerically calculated local electric field enhancements. The proposed FMTDN-functionalized AgNR SERS sensor is capable of multiplex and cross-species detection of nucleic acid and protein biomarkers with improved sensitivity, which has great potential for screening and clinical diagnosis of cancer in the early stage.

Introduction

In practical biomedical applications (e.g., clinical diagnosis), the ability to detect trace multiple disease-related biomarkers from a single biological sample in a quick and reliable manner is of high importance. Many different techniques have been developed to target this goal.^{1, 2} Among them, surface-enhanced Raman spectroscopy (SERS), with the potential to achieve single molecule detection, is very attractive and promising for multiplex detection.^{3, 4} SERS offers a unique “signature” spectral profile with very narrow spectra peaks for an individual analyte, and has been demonstrated to be able to detect trace amounts of biomarkers.⁵⁻⁸ However, in general, SERS faces two critical challenges to improving sensitivity or lowering the limit of detection (LOD), and to achieving multiplex detection. In most studies, these two challenges are targeted separately.

To improve sensitivity, researchers have paid specific attention to developing various methods to construct SERS substrates with high

enhancement factor and good reproducibility.^{9, 10} These methods include top-down strategies, such as electron beam lithography,¹¹ optical lithography,¹² nanosphere lithography,¹³ and focused-ion-beam milling;¹⁴ as well as bottom-up strategies, such as chemical synthesis,¹⁵ and assembly of metallic nano-components.¹⁶ For the past 16 years, it has been well-known that aligned silver nanorod (AgNR) arrays, fabricated by the oblique angle deposition method, can act as extremely sensitive, reproducible, and uniform SERS substrates for various analyte detections.¹⁷⁻¹⁹ To improve both the biocompatibility and sensitivity, gold or silver nanoparticles (NPs) based SERS tags have been employed. Song et al. reported sensitive sandwich immunoassays using immune-AuNP SERS tags on the SERS-active AgNR substrate for human IgG detection, with a LOD of 2.5 fg/mL.²⁰ It is suggested that using noble metal NPs or NP clusters to decorate AgNR is one way to improve sensitivity and lower the LOD, as well as to promote biocompatibility.

Currently there are two strategies to achieve multiplex chip-based SERS sensor for biomarkers such as microRNAs. One is to use an array of SERS sensors functionalized with different capture molecule probes. For example, in our previous work on the detection of multiple lung cancer-related microRNA biomarkers, different molecular beacons were assembled on different locations of an AgNR substrate to construct a sensor array.²¹ This strategy requires several SERS measurements to be performed on different functionalized regions, and the functionalization process for each probe molecule has to be optimized individually. The other strategy is to immobilize a mixture of multiple probe molecules on one SERS sensor.²² In most biomarker detections, the probe molecules are self-assembled on

^a State Key Laboratory for Organic Electronics and Information Displays & Jiangsu Key Laboratory for Biosensors, Institute of Advanced Materials (IAM), Jiangsu National Synergetic Innovation Center for Advanced Materials (SICAM), Nanjing University of Posts & Telecommunications, Nanjing 210023, China. E-mail: iamcysong@njupt.edu.cn, iamlihwang@njupt.edu.cn.

^b Department of Physics and Astronomy, University of Georgia, Athens, Georgia 30602, USA. E-mail: zhaoy@uga.edu.

^c School of Electrical and Computer Engineering, College of Engineering, University of Georgia, Athens, GA 30602, USA.

†Electronic Supplementary Information (ESI) available: See DOI: 10.1039/x0xx00000x

SERS substrate. Due to different adsorption and desorption rates, different probe molecules would result in different surface coverages and intermolecular spacings. Such an uncontrollable assembly will affect the target recognition efficiency of the target molecules and reduce the detection sensitivity. Therefore, it remains a major challenge to control the assembly of the capture DNAs on the SERS substrate.

Is there a way to simultaneously deal with the above two challenges, i.e., to achieve both higher sensitivity and multiplex detection of nucleic acids and proteins? Recently, with advances in DNA nanotechnology, self-assembled DNA structures, such as DNA framework, DNA origami and DNA tile, provide a way to concurrently assemble different capture DNAs on the same DNA superstructure with controlled spacing. For example, the tetrahedral DNA nanostructures (TDNs) assembled with several designed DNA strands and probes can intrinsically control the density and orientation of capture DNAs immobilized on the substrate.^{23, 24} Multiple capture DNAs can be easily functionalized on a single TDN for multiplex detection at the same substrate location. Thus, the multiplex detection can be achieved with a single SERS measurement, which becomes more efficient for sensing. In addition, TDNs can also be used to assemble AuNP clusters and control the gap between NPs,²⁵ which provides a method to assemble NPs on the AgNR substrate. Therefore, a strategy to use multiplex detection and NP self-assembly capabilities of DNA superstructures on AgNR substrates could provide a solution to the above two challenges simultaneously.

Here we present a proof of concept for the aforementioned strategy. A functionalized multiple-armed tetrahedral DNA nanostructures (FMTDNs)-modified AgNR array SERS substrate that can assemble AuNP clusters was constructed for the detection of multiple lung cancer-related biomarkers with improved sensitivity. The sensor can achieve single, dual, and triple biomarker detections of three lung cancer-related nucleic acid and protein biomarkers, i.e., miRNA-21, miRNA-486 and carcinoembryonic antigen (CEA) in human serum. The assembly of AuNP clusters on the AgNR array was confirmed by TEM and SEM images. The specificity and enhanced SERS performance during multiplex detection were demonstrated. The SERS enhancement model of this multiplex detection strategy has been established, the relative SERS enhancement factors qualitatively agreed with the local electric field enhancements calculated by the three-dimensional finite-difference time-domain (FDTD) method.

Experimental Section

Materials. 4-Mercaptobenzoic acid (4-MBA, 99%), 5,5'-dithiobis-(2-nitrobenzoic acid) (DTNB, 99%) and tris (2-carboxyethyl) phosphine hydrochloride (TCEP, $\geq 98\%$) were obtained from Sigma-Aldrich (Shanghai, China). 2-Mercaptobenzothiazole (2-MBT, analytical reagent), gold nanoparticles (20 nm in diameter) were purchased from Aladdin, British Biocell International (Cardiff, UK), respectively. Carcinoembryonic antigen (CEA) and neuron-specific enolase (NSE) were purchased from Shanghai Lingchao biological technology co., Ltd. (Shanghai, China). Human serum and bovine serum albumin (BSA) were obtained from Biosharp (Shenzhen, China). The single-stranded DNAs (ssDNAs), including the 6 nucleotide sequences (A-F) to construct the MTDN, capture strands (C1, C2 and C3), probe

strands (P1, P2 and P3), target miRNAs (miR-21 and miR-486), single-base mismatch miRNA (relative to miR-21) and a noncomplementary miRNA (miR-375), as listed in **Table S1**, were synthesized and HPLC-purified by Takara Biotechnology (Dalian, China). Unless otherwise specified, all the materials were used without additional purification, and sterilized ultrapure Millipore water (18.2 M Ω -cm) was used as the solvent throughout.

Several different buffers were prepared and used for the treatment of nucleic acids, including TM buffer (20 mM Tris, 50 mM MgCl₂, pH 8.0), TBE buffer (89 mM Tris, 90 mM boric acid, 2 mM EDTA, pH 8.0), TBE-Mg²⁺ buffer (89 mM Tris, 90 mM boric acid, 2 mM EDTA, 12.5 mM MgCl₂), and PBS buffer (10 mM Na₂HPO₄, 10 mM Na₂HPO₄, 100 mM NaCl, 2 mM MgCl₂, pH 7.4).

Sensing protocol. **Fig. 1** shows the general procedures for multiple-armed tetrahedral DNA nanostructure (MTDN) assembly, SERS substrate functionalization, and SERS detection. Six ssDNAs (A-F) are designed to form the MTDN structures (**Fig. 1A**), and the MTDN hybridizes with three capture DNAs (C1, C2, and C3) to form the functionalized multiple-armed tetrahedral DNA nanostructure (FMTDN). The design and self-assembly of FMTDN can be found in **Section S1** of **ES†**. Then FMTDNs are immobilized onto the AgNR array *via* the thiol functional groups at the 5' end of the selected ssDNAs to obtain the SERS-active sensor (**State (1)** in **Fig. 1B**). The functionalized AgNR substrate is incubated with the analyte mixtures containing miR-21, miR-486, and CEA, and C1, C2, and C3 on FMTDNs will capture the corresponding biomarkers (**Step (a)** and **State (2)** in **Fig. 1B**). Then, equal amount of three AuNP-based SERS-tags which also have the partially complementary probe ssDNAs to the captured biomarkers are mixed and incubated with the substrate (**Step (b)** in **Fig. 1B**). The three SERS tags are pre-prepared, and each SERS tag is designed to specifically target a particular target biomarker with a different SERS reporting molecule, i.e., the miR-21-SERS tag with the

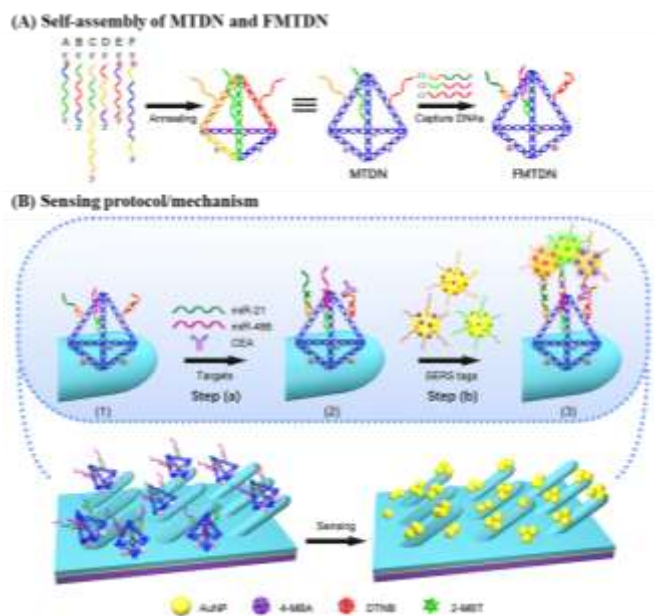


Fig. 1 (A) The functionalized multiple-armed tetrahedral DNA nanostructure self-assembly process: MTDN and FMTDN. (B) Sketch maps of the sensing protocol/mechanism of the proposed FMTDNs-modified SERS-active AgNRs array (F-AgNR SERS sensors).

Raman reporter DTNB (main peak wavenumber $\Delta\nu_{\text{DTNB}} = 1327 \text{ cm}^{-1}$), the miR-486-SERS tag with 4-MBA ($\Delta\nu_{\text{MBA}} = 1585 \text{ cm}^{-1}$), and the CEA-SERS tag with 2-MBT ($\Delta\nu_{\text{MBT}} = 1393 \text{ cm}^{-1}$). Detailed preparation and characterization of SERS tags are described in **Section S3** of **ESI†**. After the incubation with SERS tags, AuNPs or AuNP clusters (AuNP dimers and trimers) are expected to assemble onto the AgNRs to form a FMTDN-mediated target-triggered sandwich assay, and the corresponding characteristic SERS peaks of different reporter molecules (DTNB, 4-MBA, and 2-MBT) can be measured and distinguished. According to the presence of peaks at $\Delta\nu_{\text{DTNB}}$, $\Delta\nu_{\text{MBT}}$, and $\Delta\nu_{\text{MBA}}$ and the corresponding peak intensities, multiplex detection can be achieved. It is also expected that the formation of the AuNP clusters can further improve the sensitivity of the detection.

FMTDNs immobilization. The details of FMTDN formation and AgNR substrate preparation are shown in **Section S2** of **ESI†**. FMTDNs were immobilized onto the AgNRs array substrate *via* S-Ag bonds as illustrated in the **Fig. 1B**. Briefly, 20 μL of 50 nM FMTDNs solution was pipetted into each small well (well diameter of 4 mm, depth of 1 mm) patterned on the AgNRs array substrate, followed by placing into a thermostatic tank at 25°C and a humidity of $\sim 60\%$. After 3 h, the wells were washed with TM buffer thoroughly, and the FMTDNs-modified AgNRs array (F-AgNR) SERS sensors were ready for the detection of targets.

Preparation of AuNP-based SERS tags. The AuNP-based SERS tags were prepared by following our previous reports,²⁶ and the structures of three SERS tags can be seen from the magnified diagrammatic sketch shown in **Fig. 1B**. The SERS tag 1 specifically binding to miR-21 was prepared by labeling Probe-A-miR-21 and Raman reporter DTNB onto the AuNPs in sequence. Specifically, 500 μL of 2.3 nM colloidal AuNPs (20 nm) was mixed with 50 μL of 10 μM Probe-A-miR-21 in 0.5 \times TBE and incubated at 25°C for more than 4 hours. Then 12.5 μL of 2 M NaCl solution was added slowly into the mixture 4 times in 2 hours with the final concentration of NaCl reaching 200 mM, followed by aging at 25°C overnight. The Probe-A-miR-21 functionalized AuNPs were washed by 0.5 \times TBE buffer by centrifugation (9000 rpm, 20 min) for 3 times and finally re-dispersed to 500 μL . Next, 5 μL of 10 μM DTNB was added into the Probe-A-miR-21 functionalized AuNPs to label the AuNPs with DTNB molecules. After stirring for 3 h, the above mixture was purified by centrifugation three times and the final Probe-A-miR-21 and DTNB labeled AuNPs, i.e., SERS tag 1, were obtained by re-dispersing the precipitates with 50 μL PBS buffer. The preparation process of SERS tag 2 for miR-486 detection is similar to the protocol of SERS tags 1, by labeling Probe-C-miR-486 and 4-MBA onto the AuNPs in sequence. Specifically, 500 μL of 2.3 nM colloidal AuNPs (20 nm) was mixed with 50 μL of 10 μM Probe-C-miR-486, and 10 μL of 100 μM 4-MBA was added into the Probe-C-miR-486 functionalized AuNPs to label the AuNPs with 4-MBA molecules. The preparation process of SERS tag 3 for CEA detection is similar to the protocol of SERS tags 1, by labeling Probe-E-CEA and 2-MBT onto the AuNPs in sequence. Specifically, 500 μL of 2.3 nM colloidal AuNPs (20 nm) was mixed with 50 μL of 10 μM Probe-E-CEA aptamers, and 7.5 μL of 100 μM 2-MBT was added into the Probe-E-CEA functionalized AuNPs to label the AuNPs with 2-MBT molecules. The details of SERS-tag characterizations are shown in **Section S3** of **ESI†**.

Biomarkers detection. 20 μL target mixture (100 pM miR-21, 100 pM miR-486 and 100 pM CEA) was added into different F-AgNR wells and incubated in a thermostatic tank (37°C with humidity of $\sim 60\%$) for 2 h, followed by thorough PBS wash. Then, 18 μL mixed SERS tags containing equal-volume (6 μL) of miR-21-SERS tag, miR-486-SERS tag, and the CEA-SERS tag, were added into each well. After incubation in the thermostatic tank at 37°C for 3 h, the wells were washed by PBS and water subsequently. After air-drying, 20 SERS measurements at different locations in each well were performed (details see **Section S2** in **ESI†**).

FDTD calculations. A commercial software package (FDTD Solutions version 8.16.931, Lumerical Solutions Inc.) was used to calculate the localized electric field (E-field) distribution of the assembled AuNP clusters on the AgNR. The schematic of calculations is shown in **Fig. 2A**, the entire structure consists of an AgNR and three AuNP clusters (monomer, dimer, and trimer respectively) placed at the tip, middle, and bottom of the AgNR (**Fig. 2B**). The entire structure was surrounded by the dielectric environment of vacuum. The sizes and geometric parameters of AuNPs or AgNR were determined from corresponding electron microscopy images: the diameter of AuNPs was fixed to be 20 nm while the diameter and length of an AgNR were set to be 100 nm and 1 μm . The gaps between AgNR and AuNP clusters d_c were set as 0.5 nm, while the gaps between AuNPs d_p were systematically adjusted from 1 nm to 15 nm. Linearly polarized light at the wavelength of 785 nm, with a 77° angle between its propagation direction and the long axis of the nanorod, was applied, which is consistent with SERS measurement configuration. Two polarization directions, one perpendicular ($\phi = 90^\circ$) and the other parallel ($\phi = 0^\circ$) to the plane of the light propagation direction and the axis direction of nanorod, were used (**Fig. 2A**). Perfectly matched layer (PML) absorbing boundaries were used in all directions. To ensure the convergence of the calculations, a mesh size of 1 nm \times 1 nm \times 1 nm was chosen. The dielectric functions of Ag were taken from the model of Palik,²⁷ while those for Au were taken from Johnson and Christy.²⁸ A monitor of "frequency-domain field profile" was set up to calculate the localized E-field distributions and the obtained E-fields were normalized to the magnitude of the incident E-fields. The average local E-field of entire structure, including the AgNR and AuNP clusters (1 $\mu\text{m} \times 0.35 \mu\text{m}$, the orange box in **Fig. 2B**)

was calculated by $E = \sqrt{\frac{E(0^\circ)^2 + E(90^\circ)^2}{2}}$.

Results and discussion

Theoretical prediction of SERS enhancement from AuNP clusters.

The mechanism for SERS includes both EM enhancement and chemical enhancement.²⁹ However, the proposed sandwich-based detection shown in **Fig. 1**, the chemical enhancement can be neglected. Usually, chemical enhancement only occurs when there is a charge transfer between the chemisorbed molecule and the SERS substrate, or there is a severe bond deformation for a chemisorbed molecule.³⁰ This effect is very local. The SERS reporter molecules used in the experiments have already immobilized onto the AuNPs. Therefore, when the AuNPs attached to AgNR surface or form clusters, the SERS reporter molecules would remain on the original AuNPs and cannot bond to AgNR surface or another AuNP. Therefore, it is impossible to induce any chemical enhancement

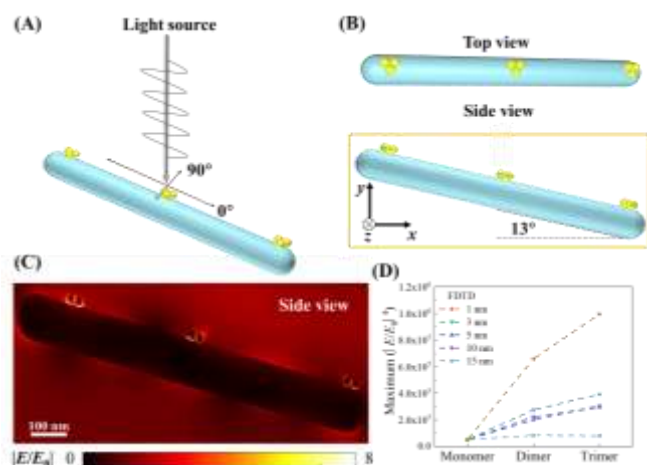


Fig. 2 (A) The schematics of FDTD calculations: AuNP dimers or trimers on the AgNR. (B) Top view and side view. (C) Representative E-field distribution of trimers (gap: 1 nm) assembled on AgNR. (D) Plots of the corresponding maximum $|E/E_0|^4$ of AuNP monomers, dimers and trimers with the gap from 1 nm to 15 nm assembled on the AgNR.

during the AuNP clustering. In addition, one shall note that there are not only EM coupling among AuNPs but also coupling from the nanogaps between the AgNRs and AuNPs. Thus, it is expected that the plasmon resonant condition is not determined by the AuNPs, but by both the AgNRs and AuNPs. In fact, our later results show that there are many AgNRs on the structure, suggesting that AgNRs would dominate the optical response of the AuNP-AgNR system. The typical absorption spectra of AgNR array substrate indicated a broad adsorption feature from 350 nm to 1200 nm.³¹ Thus, the calculated field distribution is only the consequence from the experimental excitation wavelength, i.e., 785 nm, instead of the resonance absorption wavelength of the AgNR. In fact, our previous results showed that the 785 nm excitation could produce SERS enhancement as high as 10^9 for AgNRs.¹⁷

In order to validate the proposed strategy for improved SERS sensitivity, the local E-field distribution of the assembled AuNP clusters on AgNR was first evaluated. **Fig. 2C** shows an example of a typical localized E-field distribution of the assembled AuNP trimers with $d_p = 1$ nm on the AgNR. Multiple hot spots (locations with highest local E-fields) were formed inside the nanogaps between the AuNP clusters as well as between the AuNP and AgNR. The AuNP cluster at the tip of the AgNR (upper left in **Fig. 2C**) shows the strongest hot spots, while the cluster at the bottom exhibits the slightly weaker hot spots. Since the overall SERS enhancement is approximately proportional to $|E/E_0|^4$, **Fig. 2D** plots the corresponding maximum $|E/E_0|^4$ of AuNP monomers, dimers, and trimers assembled on the AgNR from the $1 \mu\text{m} \times 0.35 \mu\text{m}$ region (**Fig. 2B**) for different d_p . Two consistent trends are observed: For the same d_p , the $|E/E_0|^4$ of the AuNP clusters increases monotonically with the AuNP number in a cluster, i.e., the trimer shows the maximum $|E/E_0|^4$; for the same cluster, the $|E/E_0|^4$ decreases monotonically with d_p . When $d_p = 15$ nm, the maximum $|E/E_0|^4$ only increases 63% from monomer to dimer, and then 55% to trimer. When $d_p = 10$ nm, the $|E/E_0|^4$ for the trimer is 6 times that of the monomer. When $d_p = 1$ nm, the $|E/E_0|^4$ of the dimer and trimer is 13 and 20 times larger than that of the monomer, respectively. Such a

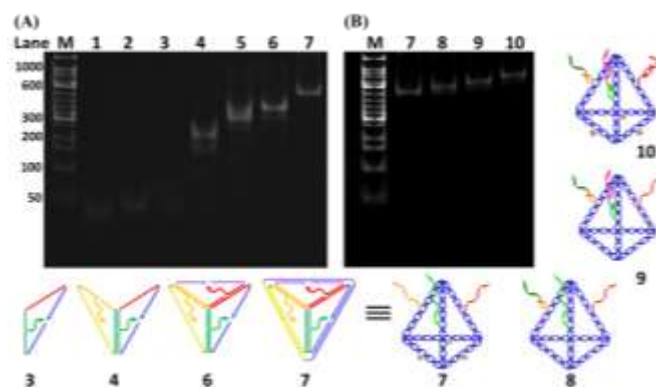


Fig. 3 Stepwise native PAGE analysis to verify self-assembly of the MTDN and FMTDN, respectively (with schematics drawn on the bottom and on the right). (A) Lane 1: A; lane 2: B; lane 3: A + B; lane 4: A+B+C; lane 5: A+B+C+D; lane 6: A+B+C+D+E; lane 7: A+B+C+D+E+F (i.e., MTDNs). (B) Lane 8: MTDNs+C1; lane 9: MTDNs+C1+C2; lane 10: MTDNs+C1+C2+C3 (i.e., FMTDNs); Marker: 50-1000 bp ladder, molecular weights of each band are shown on left. Cartoons 3-7 represent the progress of the formation of the MTDNs. The heads of the arrows represent the 3'-end of ssDNA and each color corresponds to one of the six edges of MTDN. Cartoons 8-10 (front view) represent the stoichiometric control of capture strands. The electrophoresis was run on 5% native-PAGE gel in $1 \times \text{TBE-Mg}^{2+}$ buffer with a stable voltage of 80 V in ice bath for 130 min.

small gap among the AuNP cluster is expected. According to the all-atom molecular dynamics simulation by Shen et al, when filled by ssDNAs, the average gap among the assembled AuNP clusters was 0.6 nm.³² The corresponding E-field distributions of free suspended AuNP dimers and trimers are shown in **Section S4** of **ESI†**, and the corresponding local E-field versus d_p plot (**Fig. S3B**) shows a significantly smaller $|E/E_0|^4$ compared to that of the AuNP clusters on AgNRs. Therefore, based on the FDTD results, the use of FMTDNs to control assembly AuNP clusters on the AgNR substrate has the potential to significantly enhance the intensity of SERS signal.

Characterization of FMTDN formation. As shown in **Fig. 1A**, six specially designed ssDNAs (A-F in **Table S1**) are self-assembled to form the MTDN. The detailed design description can be found in **Section S1** in **ESI†**. The 5'-ends of A, E and F ssDNAs (**Fig. 1A**) are modified with thiol groups, while three overhangs are left on three other arms to link capture strands, i.e., C1, C2, and C3, which are complementary to the targets, i.e., miR-21, miR-486, and CEA, respectively. Capture-miR-21 (C1) is divided into two parts, the underlined sequences (21-nt, green color in **Table S1**) at the 3'-end is complementary to the first overhang (green color) of the MTDNs on the sequence A; the sequences (11-nt) at the 5'-end is specially designed to capture target miR-21. A similar strategy is used to

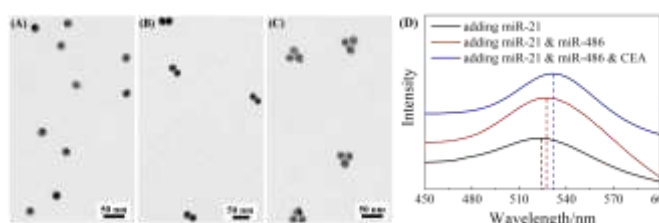


Fig. 4 TEM images of different assembled AuNPs and AuNP clusters with mixed three SERS tags by adding different biomarkers: (A) only miR-21; (B) both miR-21 and miR-486; (C) miR-21, miR-486, and CEA. (D) The UV-Vis absorption spectra of the corresponding AuNPs and AuNP clusters shown in (A)-(C), respectively.

design Capture-miR-486 (C2). For the Capture-CEA (C3), the sequence (18-nt) at the 5'-end is an aptamer, which is specially designed to capture the target CEA protein.^{33, 34} When the MTDNs hybridize with the three specially designed capture DNAs, the functionalized MTDNs (FMTDNs) are formed. The theoretical height of the MTDNs is 8 nm with equal edge lengths of 10 nm. There is a nick in the middle of each edge where the 5' and 3'-ends of the ssDNA meet. The three overhangs (21-nt) at nick on the edges is partially complementary to the three capture strands. Native polyacrylamide gel electrophoresis (PAGE) analysis (Fig. 3A) demonstrates the stepwise assembly of MTDNs as each strand was added. A distinct band shift was observed from lane 2 to 7, indicating high-yield MTDN formation were observed (lane 7). The hybridizations of three capture strands (C1, C2 and C3) were also observed from lanes 8-10 in the PAGE analysis in Fig. 3B. As the number of capture strands increases, a distinct band shift was observed due to the mobility change. Different overhang designs for site-specific capture strands hybridization allows for precise control of the number and orientation of capture strands, and their specificity to different biomarkers are detailed in Section S5 of ESI†.

AuNP cluster formation via FMTDN. The formation of AuNP clusters via FMTDNs were demonstrated in solution using the three different SERS tags. To assemble AuNP dimers, 10 nM FMTDNs were mixed with 10 nM miR-21 and 10 nM miR-486, and incubated together for 0.5 h at room temperature, followed by adding a mixture of equal amounts of miR-21-SERS tag and miR-486-SERS tag. The molar ratio of the SERS tag and FMTDNs ratio was 1.2:1. Fig. 4A and 4B show the representative TEM images of AuNP monomers and AuNP dimers formed via FMTDN assembly. The yield of the AuNP dimers was estimated to be 72%, and the average d_p in the dimers was determined to be 0.5 ± 0.2 nm. The AuNP trimers were assembled using a similar strategy, 10 nM miR-21, 10 nM miR-486, and 10 nM CEA, along with three SERS tags, were mixed and incubated. Fig. 4C shows a typical TEM image of AuNP dimers. The yield of AuNP trimers was estimated to be about 30%, and the average d_p in trimers was measured as 1.5 ± 0.3 nm. These measured d_p are consistent with those in the simulation by Shen et al.³² In addition, UV-Vis absorption spectroscopy was used to further confirm the formation of AuNP

dimers and trimers. As shown in Fig. 4D, for the AuNP monomer suspension, the localized surface plasmon resonance (LSPR) peak was centered at $\lambda_p = 523$ nm. When dimers were formed, the λ_p red-shifted to 527 nm (Fig. 4D). With the formation of AuNP trimers, the λ_p further red-shifted to 531.5 nm. The continuous redshift in λ_p further confirms the formation of dimer and trimer clusters in suspensions.

Formation of AuNP dimers and trimers on the AgNR array. The optimal condition to assemble FMTDNs onto AgNR array for SERS measurements are detailed in Section S6 in ESI† following the detection strategy shown in Fig. 1B. Under these optimal conditions, the formation of different AuNP clusters on AgNRs was investigated by SEM. When only adding miR-21 (100 pM) followed by miR-21-SERS tags (2.3 nM), as shown in Fig. 5A, almost all the AuNPs were randomly distributed and scattered all over the surface of AgNRs, and only few formed dimers and trimers. The AuNP density is $n_{AuNP}^S = 200 \pm 20 \mu\text{m}^{-2}$ and the apparent surface density of the monomer, dimers, and trimers are $n_m^S = 178 \pm 7 \mu\text{m}^{-2}$, $n_d^S = 10 \pm 3 \mu\text{m}^{-2}$, and $n_t^S = 2 \pm 1 \mu\text{m}^{-2}$, respectively. When two or three kinds of target molecules and corresponding SERS tags were added, as shown in Fig. 5B and 5C, the total number of AuNPs increases, and the AuNP dimers or trimers are consistently observed, especially in the zoomed-in images. Based on the three dimers shown in the zoomed-in image of Fig. 5B, the average d_p is determined to be 0.6 ± 0.3 nm, which is consistent with the TEM result. The densities of AuNPs, AuNP monomers, dimers, and trimers on the AgNR are estimated to be $n_{AuNP}^D = 350 \pm 30 \mu\text{m}^{-2}$, $n_m^D = 170 \pm 13 \mu\text{m}^{-2}$ and $n_d^D = 78 \pm 3 \mu\text{m}^{-2}$, and $n_t^D = 7 \pm 3 \mu\text{m}^{-2}$, respectively (Fig. 5B). From the two trimers shown in the zoomed-in image in Fig. 5C, the average d_p is 2 ± 1 nm, and the densities of AuNPs, AuNP monomers, dimers and trimers are $n_{AuNP}^T = 560 \pm 50 \mu\text{m}^{-2}$, $n_m^T = 200 \pm 11 \mu\text{m}^{-2}$, $n_d^T = 104 \pm 5 \mu\text{m}^{-2}$, and $n_t^T = 50 \pm 9 \mu\text{m}^{-2}$, respectively (Fig. 5C). Comparing Fig. 5A-C, when adding more biomarkers, the total number of AuNPs appearing on the AgNR surface becomes larger, i.e., $n_{AuNP}^D \sim 2n_{AuNP}^S$ and $n_{AuNP}^T \sim 3n_{AuNP}^S$. This result indicates that the hybridization probability of these three SERS tags is very similar regardless of the immobilization amounts of different kinds of AuNPs. In fact, Fig. 5D (solid curves) plots both the total AuNP density and the total AuNP cluster density $n_0 = n_m + n_d + n_t$ for three assembly conditions, and a monotonic increase is revealed. Fig. 5D (dashed curves) also plots the relative cluster density ratio, $\eta_i = \frac{n_i}{n_0}$, where $i = m, d, \text{ and } t$, for three assembly conditions. From single biomarker assays (only adding miR-21) to triple biomarker assays (adding miR-21, 486, and CEA), the monomer ratio η_m decreases dramatically (black dash curve), but both η_d and η_t increase (red and green dash lines), which demonstrates that (1) the FMTDNs on the AgNR surface facilitate the assembly of AuNP clusters and (2) the AuNP clusters can play a more important role in multiplex detection by SERS.

Multiplex SERS sensing performance. The sensing performance of the F-AgNR SERS sensor was evaluated for specificity and multiplex detection of the three biomarkers in 80% human serum. The performance of single biomarker detection is shown in Fig. 6A. For this assay, only a single biomarker and the mixture of three AuNP-based SERS tags were added. As a reference, the 80% human serum without spiking the biomarkers was used as the control. The nonspecific assays were carried out using the miR-375 (1 nM), a

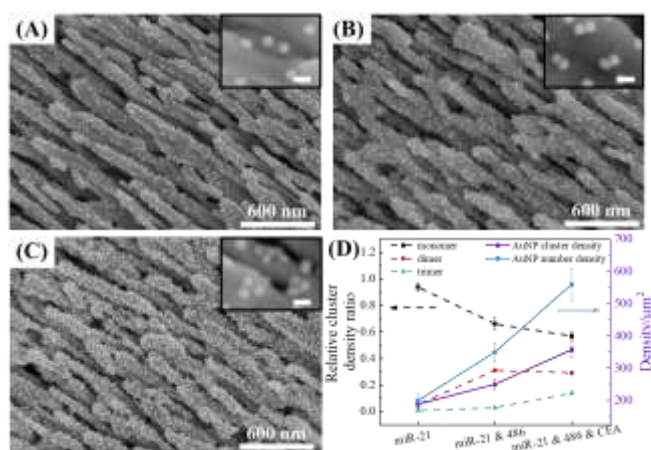


Fig. 5 SEM images: (A) adding miR-21 (100 pM); (B) adding miR-21 and miR-486 (100 pM); (C) adding miR-21, miR-486 (100 pM) and CEA (100 pM), respectively. The scale bar in the zoomed-in image: 30 nm. (D) The relative cluster density ratio, the total AuNP cluster density, and total AuNP number density for three different cases, respectively.

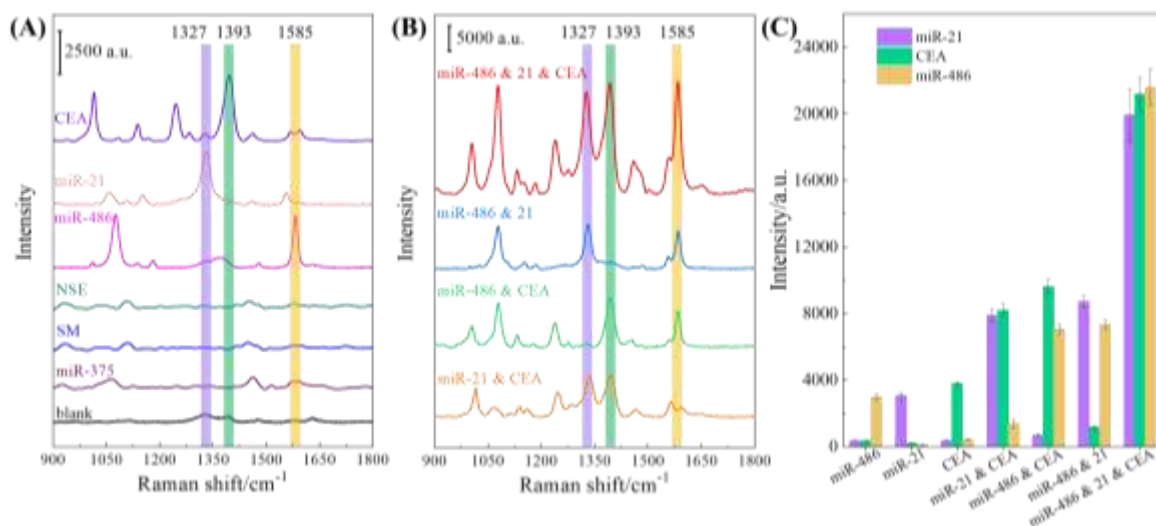


Fig. 6 (A) SERS spectra of specificity detection of analytes in human serum. (B) SERS spectra of multiplex detection of analytes in human serum. (C) Plots of corresponding Raman intensity in (B) at 1327 cm^{-1} , 1393 cm^{-1} and 1585 cm^{-1} of SERS signals.

Table 1. The SERS peak intensity ratio comparison for three detection configurations.

	Single Detection	Dual Detection			Triple Detection
		Average			
miR-21 ($\Delta\nu_{\text{DTNB}}$)	1	2.58	2.85	2.72	6.51
miR-486 ($\Delta\nu_{\text{MBA}}$)	1	2.37	2.46	2.4	7.22
CEA ($\Delta\nu_{\text{MBT}}$)	1	2.12	2.53	2.3	5.58

single-base mismatched strand relative to miR-21 (SM) (1 nM), as well as NSE protein (1 nM) in human serum. **Fig. 6A** shows the corresponding SERS spectra and the purple, green, and orange stripes indicate the characteristic peaks at $\Delta\nu_{\text{DTNB}}$, $\Delta\nu_{\text{MBA}}$, and $\Delta\nu_{\text{MBT}}$. The corresponding SERS peak intensities at $\Delta\nu_{\text{DTNB}}$, $\Delta\nu_{\text{MBA}}$, and $\Delta\nu_{\text{MBT}}$ are shown in **Fig. 6C**. For the blank control spectrum (black curve), a very weak SERS signal is observed at 1324 cm^{-1} and 1391 cm^{-1} . The peak at $\Delta\nu = 1324 \text{ cm}^{-1}$ can be assigned to ring-stretching from Adenosine,^{35,36} while the peak at $\Delta\nu = 1391 \text{ cm}^{-1}$ may result from unknown contamination from the environment (**Fig. S10**). Similarly, weak SERS spectra were obtained in the nonspecific target groups of miR-375, SM, and NSE, suggesting that different non-specific biomolecules (i.e., other miRNAs, or proteins, etc.) could not provide interference sensing signals. The variation in the detailed spectra features for these four cases may be due to nonspecific binding of biomolecules on the F-AgNR SERS sensor, while the probability of nonspecific binding of SERS tags is very small as revealed in the SERS spectra. However, when the F-AgNR SERS sensor was treated with miR-21, miR-486, and CEA, respectively, distinguished SERS peaks at $\Delta\nu_{\text{DTNB}}$, $\Delta\nu_{\text{MBT}}$ and $\Delta\nu_{\text{MBA}}$, were observed, as shown in **Fig. 6A**. After treatment with 100 pM miR-21, the peak at $\Delta\nu_{\text{DTNB}} = 1327 \text{ cm}^{-1}$ appears in **Fig. 6A**. Similarly, after treatment with 100 pM miR-486 or 100 pM CEA, distinctive peaks at $\Delta\nu_{\text{MBA}}$ or $\Delta\nu_{\text{MBT}}$ appear, which indicates the successful recognition of the specific biomarkers and capture corresponding SERS tags, as designed. The intensities plotted

in **Fig. 6C** demonstrate the same trend. Thus, the results in **Fig. 6A** demonstrate that the F-AgNR SERS sensor is only specific to biomarkers of miR-21, miR-486, and CEA.

Dual and triple biomarker assays were carried out and the results are plotted in **Fig. 6B**. In dual detections, three dual biomarker combinations were used: 100 pM miR-21 and 100 pM CEA, 100 pM miR-486 and 100 pM CEA, as well as 100 pM miR-21 and 100 pM miR-486. According to the design, one expects to observe two distinguished SERS peaks from $\Delta\nu_{\text{DTNB}}$, $\Delta\nu_{\text{MBT}}$ and $\Delta\nu_{\text{MBA}}$. In fact, this is true as revealed in **Fig. 6B**: when the miR-21 and CEA mixture was tested, two SERS tag peaks at $\Delta\nu_{\text{DTNB}}$ and $\Delta\nu_{\text{MBT}}$ were observed; when the miR-486 and CEA mixture was assayed, two peaks at $\Delta\nu_{\text{MBA}}$ and $\Delta\nu_{\text{MBT}}$ appear; and for the test of miR-21 and miR-486 mixture, two peaks at $\Delta\nu_{\text{DTNB}}$ and $\Delta\nu_{\text{MBA}}$ emerge. The peak intensities of these three peaks under the three different conditions plotted in **Fig. 6C** confirm the observation. However, compared to the single biomarker detection, the peak intensities at the corresponding SERS tag wavenumbers for dual biomarker detection are roughly almost doubled. The triple biomarker detection was performed using a mixture of 100 pM miR-21, 100 pM miR-486 and 100 pM CEA, and the corresponding SERS spectrum is shown in **Fig. 6B** (red curve). As expected, all three distinguished SERS peaks at $\Delta\nu_{\text{DTNB}}$, $\Delta\nu_{\text{MBT}}$ and $\Delta\nu_{\text{MBA}}$, are observed. The corresponding SERS intensity plotted at $\Delta\nu_{\text{DTNB}}$, $\Delta\nu_{\text{MBT}}$ and $\Delta\nu_{\text{MBA}}$ in **Fig. 6C** shows that the corresponding intensity in triple biomarker detection is nearly 5-7 times of the single biomarker detection.

Above results can be briefly understood as the following: The functionalized AuNP is acting as a SERS tag. When the SERS tag is hybridized on the AgNR substrate, the SERS signal of the Raman report molecules will be enhanced due to the enhancement of AgNR. In addition, during the multiplex detection, the AuNP clusters are formed, and an additional SERS enhancement is achieved as demonstrated in **Fig. 6**. The SERS responses of the three as-prepared SERS tags were characterized by dispensing 20 μL SERS tag suspension into PMDS wells on a silicon substrate respectively and after air-drying SERS measurements were performed and the corresponding Raman spectra are shown in **Fig. S2** of ESI† (785 nm

wavelength, 177.2 mW laser power, 5 s acquisition time). The surface AuNP density was estimated to be $\sim 2.2 \times 10^4$ particle/ μm^2 . Then based on **Fig. 5A**, the AuNP density on AgNR was estimated to be ~ 189 particle/ μm^2 . The SERS measurements were performed with 785 nm wavelength, 9 mW laser power, 2 s acquisition time. Thus, the SERS signal per AuNP particle on AgNR was 1164 times as large as that on Si substrate, indicating a strong enhancement of AuNP tag by the AgNR substrate.

In addition, other performance parameters of the sensor, such as uniformity and reproducibility, have been characterized as shown in **Section S7** of **ESI†**. The results show that the F-AgNR SERS sensors are highly uniform, the SERS signal variations for all three SERS tags are less than 9%, and 6 batches of AgNR substrates only produce < 8.3% variation in different detection signals, i.e., the sensors are highly reproducible. Therefore, based on the above results, the following four conclusions can be drawn: (1) The designed F-AgNR SERS sensor is only specific to biomarkers of miR-21, miR-486, and CEA; (2) The sensor can achieve single, dual and triple biomarker detections; (3) With the same concentration of the biomarker, the SERS intensity of the SERS tag peak with respect to the corresponding biomarker increases significantly when the detection changes from single to dual, then to triple biomarker detection; and (4) The sensors are very uniform and highly reproducible.

However, due to the additional clustering induced enhancement in multiplex detection, quantitative detection based on this strategy is quite challenge. For example, even the miR-486 concentration will be fixed, and its respective SERS tags produce a certain amount of SERS signal on AgNR substrate, but when the FMTDN further hybridized with the SERS tags for CEA, or together with SERS tags for CEA and miR-21, the SERS signal for miR-486 would be more than doubled or even as high as 7 times according to **Fig. 6**. However, the total amount of the SERS tags of miR-486 on the AgNR substrate was not changed. Thus, the quantitation is impossible by just examining the intensity of the characteristic SERS peak. However, machine learning (or deep learning) could be an excellent solution for this, if the spectra of a suitable number of selective mixture of biomarkers with different mixing ratio and concentrations could be used as modeling spectral set to adapt an appropriate algorithm.³⁷⁻³⁹

Understanding the SERS intensity changes due to multiplex detection or AuNP clustering. In the above conclusions, the third point needs to be further understood. **Table 1** summarizes the intensity ratio to the single biomarker detection at corresponding Δ_{VDTNB} , Δ_{VMBT} and Δ_{VMBA} for the single, dual, and triple biomarker detection configurations. For the dual biomarker detection, the corresponding SERS peak intensity is 2.3-2.7 times that of single biomarker detection while this ratio jumps to 5.58-7.22 for triple biomarker detection. Such a significant increase in SERS intensities can only come from two possible sources: the number of SERS tags corresponding to specific biomarker is increased or the SERS enhancement factor increases significantly. According to **Fig. 5D**, the AuNP densities n_{AuNP} for single (n_{AuNP}^S), dual (n_{AuNP}^D), and triple (n_{AuNP}^T) biomarker detection satisfy the following relationship, i.e., $n_{\text{AuNP}}^D \approx 2n_{\text{AuNP}}^S$ and $n_{\text{AuNP}}^T \approx 3n_{\text{AuNP}}^S$. Since each SERS tag only carries one kind of Raman report molecules, it is concluded that when the detection configuration changes from single to dual biomarker detection, the extra AuNPs on the F-AgNR SERS sensor are all coming from different AuNP-based SERS tags. A similar conclusion

can be drawn for triple biomarker detection. That is, if the three detection configurations have one of the same biomarkers, then the surface densities of AuNP-based SERS tag for that biomarker at these three conditions are the same, i.e., the amount of Raman reporter molecules is roughly the same for all three configurations. Therefore, the enhanced intensity shown in **Table 1** can only come from SERS enhancement factor change.

For a fixed biomarker in single, dual, and triple biomarker detection configurations, the corresponding SERS peak intensity can be written as,

$$I^S \propto E_m n_m^S + 2E_d n_d^S + 3E_t n_t^S, \quad (1)$$

$$I^D \propto \frac{1}{2}E_m n_m^D + E_d n_d^D + \frac{3}{2}E_t n_t^D, \quad (2)$$

$$I^T \propto \frac{1}{3}E_m n_m^T + \frac{2}{3}E_d n_d^T + E_t n_t^T, \quad (3)$$

where E_m , E_d , E_t are the SERS enhancement factors of AuNP monomers, dimers, and trimers on AgNR, respectively; the superscript, S, D , and T , represents different detection configuration, and n_m^i , n_d^i , n_t^i are cluster densities of monomer, dimer and trimer on AgNR, respectively. The factors 2 and 3 in **Eq. 1** are due to the amount of SERS tags carried by different cluster. If an AuNP monomer carries one part of the tags, then the AuNP dimer consisting of the same SERS tags have two parts of tags, and so on. The 1/2 factor in **Eq. 2** and 1/3 in **Eq. 3** for monomer intensity for dual and triple detections are due to our assumption that the monomers have equal number of other SERS tags. The 3/2 and 2/3 factor in **Eqs. 2** and **3** are the probabilities of the number of the same SERS tag inside a particular cluster. Setting $\frac{I^D}{I^S} = 2.5$, $\frac{I^T}{I^S} = 6.4$, and taking the data for the cluster density from **Fig. 5D**, we obtain that $\frac{E_d}{E_m} = 150$ and $\frac{E_t}{E_m} = 840$. This result shows that the AuNP cluster on the AgNR substrate not only provides a way to achieve multiplex detection, but also significantly enhances the SERS signal. In fact, recalling the FDTD results from **Fig. 2D**, for $d_p = 1$ nm, the $|E/E_0|^4$ of the dimer and trimer is 13 and 20 times that of the monomer, respectively, which is qualitatively consistent with the experimental result. The discrepancy in the magnitude may result from the effect of AgNR arrays on the AuNP clusters.

Conclusions

In a summary, the FMTDNs-modified AgNR array substrate is demonstrated for multiplex detection of three lung cancer-related biomarkers, i.e., miR-21, miR-486 and CEA protein with enhanced SERS signals. The SERS signals of a particular SERS tag are not only enhanced due to AgNRs, but also the hybridization induced clustering of AuNPs gives an additional enhancement. The sensor is highly specific to the three biomarkers. The high sensitivity and good specificity for FMTDNs-based SERS sensor is attributed to the following advantages: (1) The FMTDNs provide a template to align the probe molecules upright on the AgNR surfaces; the MTDNs with high rigidity allow themselves to immobilize on the Ag surface with upright orientation. This could avoid possible steric crowding and electrostatic interaction often encountered by soft ssDNA probes,⁴⁰ thus results in high hybridization efficiency for target molecules; (2) The assembled FMTDNs on the surface provide an appropriate space

among adjacent probe molecules for high efficacy hybridization: the FMTDN, with triangular pyramid structure plus a six-carbon spacer, theoretically forms a biomolecule layer (~ 8 nm thick) on the AgNRs.⁴¹ Such a structure can provide a liquid-phase-like environment to enhance the hybridization efficiency with target molecules, resulting in high capture efficiency of target molecules; (3) The self-assembled AuNP clusters on the FMTDNs can provide extra hot spots on the AgNR surface for SERS enhancement: the spatial arrangement of AuNPs based on FMTDNs achieved a small interparticle distance, < 2 nm, in the presence of biomarkers, facilitating an effective plasmonic coupling and, in turn, generated a high density of hot spots for SERS enhancement; (4) Large surface area of AgNR: the AgNR array substrates with large surface areas and rough surface topographies provide more space for assembling more FMTDNs so as to enhance the ability to capture SERS tags. With these advantages, the proposed DNA nanostructure functionalized AgNR SERS sensor shows a great potential for screening and clinical diagnosis of cancer in the early stage.

Author Contributions

The manuscript was written through the contributions of all authors. All authors have given approval to the final version of the manuscript.

Conflicts of interest

The authors declare no competing financial interest.

Acknowledgements

Chunyuan Song, Jingjing Zhang, Jie Chao, and Lianhui Wang were supported by the National Key Research and Development Program of China (2017YFA0205300), National Natural Science Foundation of China (61871236) and Qinglan Project of Jiangsu Province of China. Yanjun Yang, Hoang Mai Luong, and Yiping Zhao were partially supported by a National Science Foundation grant under the Grant No. ECCS-1808271. We would like to thank Mr. Yoong Sheng Phang and Mr. James Haverstick for proofreading this manuscript.

References

1. M. Ferrari, *Nature Reviews Cancer*, 2005, **5**, 161-171.
2. Y. Shen, Y. Zhang, Z. F. Gao, Y. Ye, Q. Wu, H.-Y. Chen and J.-J. Xu, *Nano Today*, 2021, **38**, 101121.
3. K. Kneipp, Y. Wang, H. Kneipp, L. T. Perelman, I. Itzkan, R. R. Dasari and M. S. Feld, *Physical Review Letters*, 1997, **78**, 1667.
4. S. Nie and S. R. Emory, *Science*, 1997, **275**, 1102-1106.
5. M. D. Porter, R. J. Lipert, L. M. Siperko, G. Wang and R. Narayanan, *Chemical Society Reviews*, 2008, **37**, 1001-1011.
6. S. P. Mulvaney, M. D. Musick, C. D. Keating and M. J. Natan, *Langmuir*, 2003, **19**, 4784-4790.
7. J. Kneipp, H. Kneipp, B. Wittig and K. Kneipp, *Nanomedicine: Nanotechnology, Biology and Medicine*, 2010, **6**, 214-226.
8. Y. Pang, C. Wang, J. Wang, Z. Sun, R. Xiao and S. Wang, *Biosensors and Bioelectronics*, 2016, **79**, 574-580.
9. J. Fang, S. Du, S. Lebedkin, Z. Li, R. Kruk, M. Kappes and H. Hahn, *Nano Letters*, 2010, **10**, 5006-5013.
10. K. Zhang, J. Zhao, H. Xu, Y. Li, J. Ji and B. Liu, *ACS Applied Materials & Interfaces*, 2015, **7**, 16767-16774.
11. N. A. Abu Hatab, J. M. Oran and M. J. Sepaniak, *ACS Nano*, 2008, **2**, 377-385.
12. T. Y. Jeon, S.-G. Park, D.-H. Kim and S.-H. Kim, *Advanced Functional Materials*, 2015, **25**, 4681-4688.
13. X. Zhao, J. Wen, M. Zhang, D. Wang, Y. Wang, L. Chen, Y. Zhang, J. Yang and Y. Du, *ACS Applied Materials & Interfaces*, 2017, **9**, 7710-7716.
14. T. Gao, Z. Xu, F. Fang, W. Gao, Q. Zhang and X. Xu, *Nanoscale Research Letters*, 2012, **7**, 399.
15. C. Song, N. Zhou, B. Yang, Y. Yang and L. Wang, *Nanoscale*, 2015, **7**, 17004-17011.
16. J. Sun, R. Liu, J. Tang, Z. Zhang, X. Zhou and J. Liu, *ACS Applied Materials & Interfaces*, 2015, **7**, 16730-16737.
17. J. D. Driskell, S. Shanmukh, Y. Liu, S. B. Chaney, X. J. Tang, Y. P. Zhao and R. A. Dluhy, *The Journal of Physical Chemistry C*, 2008, **112**, 895-901.
18. Y. J. Liu and Y. P. Zhao, *Physical Review B*, 2008, **78**, 075436.
19. Y.-J. Liu, Z.-Y. Zhang, Q. Zhao, R. Dluhy and Y.-P. Zhao, *The Journal of Physical Chemistry C*, 2009, **113**, 9664-9669.
20. C. Song, J. Chen, Y. Zhao and L. Wang, *Journal of Materials Chemistry B*, 2014, **2**, 7488-7494.
21. C. Song, Y. Yang, B. Yang, Y. Sun, Y. P. Zhao and L.-H. Wang, *Nanoscale*, 2016, **8**, 17365-17373.
22. R. Guo, F. Yin, Y. Sun, L. Mi, L. Shi, Z. Tian and T. Li, *ACS Applied Materials & Interfaces*, 2018, **10**, 25770-25778.
23. H. Pei, X. Zuo, D. Zhu, Q. Huang and C. Fan, *Accounts of Chemical Research*, 2014, **47**, 550-559.
24. M. Lin, J. Wang, G. Zhou, J. Wang, N. Wu, J. Lu, J. Gao, X. Chen, J. Shi and X. Zuo, *Angewandte Chemie International Edition*, 2015, **54**, 2151-2155.
25. L. Xu, W. Yan, W. Ma, H. Kuang, X. Wu, L. Liu, Y. Zhao, L. Wang and C. Xu, *Advanced Materials*, 2015, **27**, 1706-1711.
26. B. Liu, C. Song, D. Zhu, X. Wang, M. Zhao, Y. Yang, Y. Zhang, S. Su, J. Shi, J. Chao, H. Liu, Y. Zhao, C. Fan and L. Wang, *Small*, 2017, **13**, 1603991.
27. W. Choyke and E. D. Palik, *Palik (ed.), Academic Press, Inc*, 1985, **587**.
28. P. B. Johnson and R.-W. Christy, *Physical Review B*, 1972, **6**, 4370.
29. X. Wang, S.-C. Huang, S. Hu, S. Yan and B. Ren, *Nature Reviews Physics*, 2020, **2**, 253-271.
30. T.-H. Park and M. Galperin, *Physical Review B*, 2011, **84**, 075447.
31. Y. P. Zhao, S. B. Chaney and Z. Y. Zhang, *Journal of Applied Physics*, 2006, **100**, 063527.
32. J. Shen, B. Luan, H. Pei, Z. Yang, X. Zuo, G. Liu, J. Shi, L. Wang, R. Zhou, W. Cheng and C. Fan, *Advanced Materials*, 2017, **29**, 1606796.
33. G. R. H. Tabar and C. L. Smith, *World Applied Sciences Journal*, 2010, **8**, 16-21.
34. *United States Pat.*, 2010.
35. L. Guerrini, Ž. Krpetić, D. van Lierop, R. A. Alvarez - Puebla and D. Graham, *Angewandte Chemie*, 2015, **127**, 1160-1164.
36. J. L. Abell, J. M. Garren, J. D. Driskell, R. A. Tripp and Y. Zhao, *Journal of the American Chemical Society*, 2012, **134**, 12889-12892.
37. H. He, S. Yan, D. Lyu, M. Xu, R. Ye, P. Zheng, X. Lu, L. Wang and B. Ren, *Analytical Chemistry*, 2021, **93**, 3653-3665.

38. N. M. Rabovsky and I. K. Lednev, *Chemical Society Reviews*, 2020, **49**, 7428-7453.
39. F. Lussier, V. Thibault, B. Charron, G. Q. Wallace and J.-F. Masson, *TrAC Trends in Analytical Chemistry*, 2020, **124**.
40. M. H. Lin, J. J. Wang, G. B. Zhou, J. B. Wang, N. Wu, J. X. Lu, J. M. Gao, X. Q. Chen, J. Y. Shi, X. L. Zuo and C. H. Fan, *Angewandte Chemie-International Edition*, 2015, **54**, 2151-2155.
41. H. Pei, N. Lu, Y. Wen, S. Song, Y. Liu, H. Yan and C. Fan, *Advanced Materials*, 2010, **22**, 4754-4758.